Supporting Information for

Direct measurement of interhelical DNA repulsion and attraction by quantitative crosslinking

Ian Hamilton[1], Magdalena Gebala[2], Daniel Herschlag[2], and Rick Russell[1,*]

[1]Department of Molecular Biosciences, University of Texas at Austin, Austin, TX 78712

[2]Department of Biochemistry, Stanford University, Stanford CA 94305

*Corresponding author

Email: rick_russell@cm.utexas.edu

https://orcid.org/0000-0002-4879-8563
https://orcid.org/0000-0002-6217-9013

This file includes:

Supporting Text

Supporting Figures S1 to S13

Supporting Tables S1

Supporting Text

Estimation of average linker extensions

The manufacturers of the reagents we used to generate thiol- and disulfide modified DNA (Fig. S1) provide documentation which includes size estimates of the molecules. From this information, we estimated ~10 Å and ~20 Å for the lengths of the short and long linkers, respectively. To test the manufacturer's estimates, we modeled the short linkers as simple freely rotating self-avoiding walks (SAWs) fixed at one end to an impenetrable surface (the helix) with parameters appropriate for C-C bonds (Fig. S2A). We wrote a program in Python that returned statistics for the predicted extension of the chain end from its connection point, allowing the construction of a probability distribution function (PDF) for the chain extension (Fig. S2B, red curve). For a chain of 14 segments, corresponding to our short linker, this unperturbed SAW has an average extension of 9.46 Å (calculated as an expectation value from the PDF), similar to the estimate based on the manufacturer's documentation.

Additionally, because the thiol is fractionally deprotonated and thus charged, the electrostatic potential of the attached helix (modeled by PB in Fig. S2B, blue points) should perturb the PDF for finding the chain end with the thiol moiety. Chains with shorter extensions experience a more negative potential, and thus disfavor the negatively charged thiolate, while motions of the chain that move the thiol farther from the helix would be more easily deprotonated, biasing the distribution toward larger extensions. We used PB calculations for the electrostatic potential at various salt concentrations to estimate the free energy penalty for finding a deprotonated thiolate across chain extensions and Boltzmann-weighted our SAW PDF to yield electrostatically perturbed PDFs for the thiol-modified chains (Figs. S2C, D; Na^+ and Mg^{2+}, respectively). We found that the PDFs were modestly perturbed, with average chain extension increasing by <2 Å at our lowest ionic strength and trending towards the unperturbed chain with increasing salt concentration (Fig. S2E). Based on this modeling, the approximation from manufacturer's documentation remains reasonable.

Lastly, we validated this SAW/PB model by comparing the predicted thiol pK_a values with those measured experimentally by disulfide exchange (Figs. S2F, G). The electrostatic penalty on thiol deprotonation imposed by the electrostatic potential of the helix shifts the thiol pK_a from its intrinsic value free in solution, dependent on both salt concentration and distance from the helix (*i.e.,* chain extension). To provide a reference for the intrinsic thiol pK_a, we measured the pK_a of the small molecule N-phenyl-3-sulfanylpropanamide, a structural analog of the thiol moiety found at our linker termini (Fig. S5). With this free solution reference pK_a as the unperturbed baseline, we used the electrostatic potential computed by PB to estimate the magnitude of the pK_a shift across chain extensions, and then we used the electrostatically perturbed PDFs discussed above to compute an ensemble pK_a at various salt concentrations. The pK_a values calculated in this way are reasonably consistent with those measured for the thiolated helix by disulfide exchange with 2-aldrithiol (see *Determination of the salt dependences of K_a and k_{chem}* and Fig. 3 in main text), though the model tends to modestly underestimate the pK_a at lower salt concentrations. Taken together, these pK_a data are consistent with the linker length for the short linkers determined from manufacturers' documentation, ~10 Å.

Assessing the impact of helix encounters on observed pK_a

Measurements with 2-aldrithiol were designed to yield the pK_a of the thiol on an isolated DNA helix. This situation corresponds to the order of kinetic steps of the crosslinking reaction outlined in Fig. 2B, wherein the thiol deprotonation occurs in the ground state, followed sequentially by helical encounter and disulfide exchange. In principle, the thiol deprotonation (K_a) and helical encounter (K_{enc}) steps may also occur in the opposite order (Fig S6A, bottom path), as both steps are in rapid equilibrium relative to disulfide exchange. In this opposite order, it is tempting to imagine that the presence of the second helix will, by substantially changing the local electrostatic potential (Fig 1G-L), perturb the pK_a of the thiol ($K_{a,isol} \neq K_{a,dual}$). Because we are using information about the thiol pK_a to isolate salt dependences on K_{enc}, and we cannot directly measure the pK_a of the thiol during a helical encounter, it is important that we verify the validity of using only the pK_a for the isolated helix.

We expect that because we are well below saturation of K_{enc} under our experimental conditions, we need only consider the pK_a in the ground state; *i.e.,* the pK_a of the isolated helix. To confirm this point for our crosslinking reactions, we performed numerical kinetic simulations using KinTek Explorer [1] of the full reaction scheme shown in Fig S6A. KinTek Explorer automatically models protonation/deprotonation steps as diffusion-controlled rapid

equilibria with user-specified pK_a values. For kinetic parameters making up $K_{enc,deprot}$ and $K_{enc,prot}$, we assumed near-diffusion limited association (10^8 M^{-1} s^{-1}) and corresponding dissociation rate constants that satisfied our calculated bounds on k_{chem} and K_{enc} (see *Establishment of bounds on* k_{chem}) and maintained all equilibria in rapid equilibrium relative to k_{chem}. Additionally, all kinetic rates and equilibria were selected to enforce closure of the thermodynamic cycle of states 1-4.

Under these constraints, we performed simulations with several combinations of $K_{a,isol}$ and $K_{a,dual}$ (Fig S6B). These simulations were time courses performed at disulfide helix concentrations of $0.1 - 2$ μM across the pH range 6 – 12. At each pH, simulated time course data was fit as for our experiments (Fig 2C,D) to obtain second-order rate constants for crosslinking (Fig S6B, blue circles). Fitting these data to Henderson-Hasselbalch curves (dashed lines) reveals that in each case, the apparent pK_a is equal to $pK_{a,isol}$. Thus, the value of $pK_{a,dual}$ makes no perceptible difference to the observed rate constants or the observed pK_a, confirming the expectation above that the relevant parameter is the thiol pK_a in the context of the isolated helix.

These observations can be rationalized by considering the free energy differences among the states 1-4 (Fig S6C). Our experiments are operating reasonably close to the pK_a ($|pK_a - pH| \leq 1$), while our helix concentrations are orders of magnitude below saturation, so the free energy differences between states {1,4} and {3,2} are modest, while those between {1,3} and {4,2} are quite large. Consequently, the free energy difference between states 3 and 4 is large, and so state 4 is expected to be relatively unpopulated compared to state 3. It follows that the two equilibria directly involving state 4 ($K_{enc,prot}$ and $K_{a,dual}$) are also relatively unpopulated. In contrast, state 3 is relatively highly populated, and so the equilibria involving state 3 ($K_{a,isol}$ and $K_{enc,deprot}$) are also populated. From this and the simulation results, we conclude that the relevant pK_a in our crosslinking reactions is $pK_{a,isol}$, and that we need not consider the bottom path in Fig S6A.

Establishment of bounds on k_{chem}

While we were unable to measure the first-order disulfide exchange rate constant k_{chem}, we were able to establish lower and upper bounds. A conservative lower bound was established from the observed pseudo-first-order crosslinking rate constants. Consider that the observed rate of a multi-step reaction cannot exceed the rate of any one of its constituent first-order kinetic steps. Therefore, an absolute lower bound on k_{chem} is the largest pseudo-first-order crosslinking rate we observed, normalized to consider only the reaction from the deprotonated thiolate. This lower bound is $k_{chem} > k_{obs,max} \approx 2$ s^{-1}, and was obtained from interhelical crosslinking reactions performed at pH 8.0 (100 mM Tris) with 15 mM Co(NH$_3$)$_6$Cl$_3$ with 20 μM disulfide helix. This value is firmly established as a lower bound, but the fact that we are far below saturation at 20 μM disulfide helix means that it is likely much lower than the value of k_{chem}.

As an alternative approach, we considered diffusion kinetics to provide both lower and upper bounds on the value of k_{chem}. In this approach, we take our maximal second-order rate constant with 2-aldrithiol, $k_{max} = 1.3 \times 10^4$ M^{-1} s^{-1}, to be the second-order reaction rate constant between the disulfide and the thiolate (*i.e.*, $k_{max} = K_{enc} \times k_{chem}$). Assuming that the process of bringing two helices close enough for crosslinking is controlled by diffusion (K_{enc}), we can estimate the diffusion-controlled encounter equilibrium ($K_{enc,diff}$) to establish an estimate of k_{chem}.

First, we estimate the association rate constant k_{assoc} using the well-known relation for diffusion-limited processes:

$$k_{assoc} = 8\pi D r$$

where r is a characteristic length scale for the reaction, intuitively the center-to-center distance between molecules at the instant of reaction, and D is a diffusion constant. This equation gives the rate of bimolecular collision for molecules in free diffusion, and in aqueous solution is generally $\sim 10^9$-10^{10} M^{-1} s^{-1}.

The dissociation rate constant k_{diss} can be estimated as the inverse of the residence time of the molecules in a "collided" state. For this residence time, we take the characteristic timescale for random walk diffusion over a length scale r in three dimensions:

$$\frac{1}{k_{diss}} = \frac{r^2}{6D}$$

This equation can be understood as the first-order rate constant for diffusion out of reaction range from a reaction partner. The two equations above are combined to give an expression for $K_{enc,diff}$:

$$K_{enc,diff} = \frac{k_{assoc}}{k_{diss}} = \frac{4\pi r^3}{3}$$

The right side of the equation above represents simply the volume of a sphere of radius r, or the volume around each molecule where a reaction is permitted by proximity. With Avogadro's number as a conversion factor, this has the units of an equilibrium association constant (M^{-1}), and can be thought of as the average number of reactive molecules in a sphere of radius r per molar.

Bounds on $K_{enc,diff}$ may therefore be established by estimating r, the effective "range" of the reaction. Here we take as lower and upper bounds the radius of the DNA helix, ~5 Å, and the helical radius plus the contour length of the fully extended probe linker, ~25 Å, respectively. From these bounds of the length scale of the reaction, we obtain bounds on the diffusion-dominated encounter equilibrium, 0.3 M^{-1} < $K_{enc,diff}$ < 40 M^{-1}. Finally, using the experimentally determined maximal second-order rate constant k_{max}, we obtain bounds on the rate of chemistry 330 s^{-1} < k_{chem} < 4.3 × 10^4 s^{-1}. Our actual estimate of the probe linker distribution (Fig. S2B), with a radius of gyration of ≈ 8.4 Å, implies values of $K_{enc,diff}$ ≈ 1.5 M^{-1} and k_{chem} ≈ 8700 s^{-1}. As these estimates for k_{chem} are all orders of magnitude lower than the expected values for the diffusion-controlled rate constants k_{assoc} and k_{diss}, the encounter equilibrium K_{enc} is in rapid equilibrium with respect to disulfide formation. Equivalently, k_{chem} is the rate-limiting step.

Poisson-Boltzmann calculations of ΔG$_{elec}$

We used Poisson-Boltzmann (PB) calculations to estimate the electrostatic free energy penalty of interhelical approach, ΔG_{elec} (Fig S8). Specifically, we used PB to calculate the electrostatic energy of a pair of helices separated by 20 Å (as measured from linker connection points) relative to the electrostatic energy calculated for a pair of isolated helices (Fig S8A) across the range of salt concentrations covered in our experiments. While PB is usually applied to the calculation of state energies where a preferred molecular conformation is known *a priori*, we cannot know the relative orientation of the helices in our case. We therefore performed electrostatic energy calculations using several relative orientations of the helices (Fig. S8B) and calculated a Boltzmann ensemble average over these orientations, taking this frequency-weighted average as our estimate of ΔG_{elec} (Fig S8C,D, solid curves; Fig 5, solid curves). Boltzmann ensembles are naturally dominated by energetically favorable states because such states are also the most probable. Because the electrostatic free energy penalty depends rather sharply on the relative orientation of the helices, we were able to construct a representative ensemble by selecting states emphasizing 'off-axis' orientations that limit proximity of backbone charges, representing electrostatic free energy minima. In this way, we constructed a representative ensemble from a relatively small number of energetically favorable states. Our ensemble also included an energetically unfavorable parallel orientation (Fig S8B, top left), and as expected, we find that this state makes a vanishingly small contribution to ΔG_{elec}.

These calculations show substantial divergence between ΔG_{elec} and the measured value of the free energy penalty for interhelical encounters, ΔG_{enc} (Fig 5, solid curves vs. points). In general, PB predicts that the electrostatic penalty is substantially larger than that observed. PB predicts much steeper log-linear NaCl dependence for ΔG_{elec} (slope 2.80, CI_{95}[2.62, 2.98]) than experimentally observed for ΔG_{enc} (slope 0.87, CI_{95}[0.68, 1.15]). While the log-linear $MgCl_2$ dependence is only modestly steeper for ΔG_{elec} (slope 1.28, CI_{95}[1.24, 1.31]) than observed for ΔG_{enc} (slope 0.96, CI_{95}[0.78, 1.22]), PB places the transition to the screening regime at a $MgCl_2$ concentration an order of magnitude higher than that observed experimentally. This lack of correspondence between ΔG_{elec} and ΔG_{enc} implies either that PB fails to accurately model the electrostatics or that ΔG_{enc} is not strictly dominated by electrostatics, suggesting the existence of an additional energy term in ΔG_{enc}.
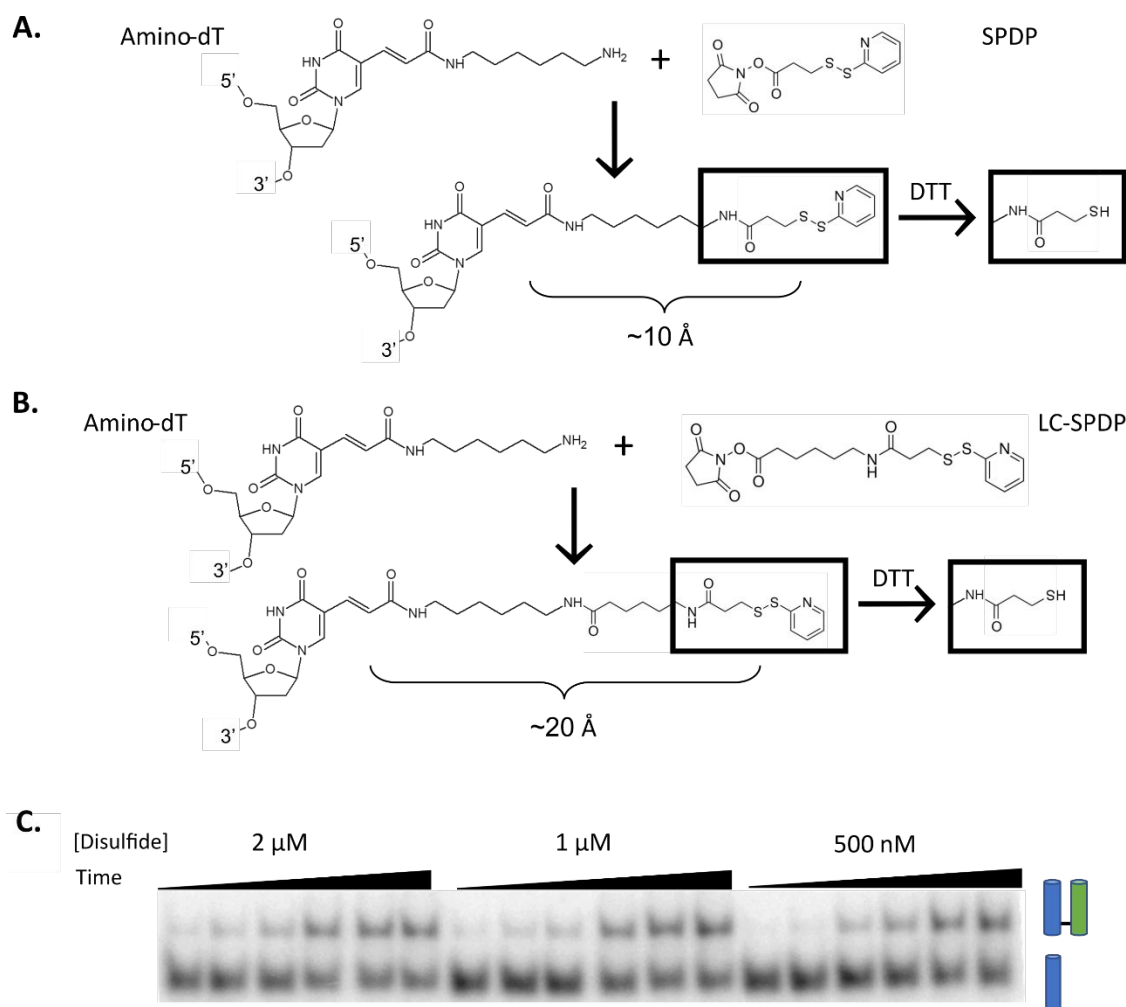
Supporting Figures

Figure S1. Modified helices are prepared via NHS chemistry between amino-dT-modified oligonucleotides and either A) SPDP or B) LC-SPDP, in each case yielding a terminal dipyridyl disulfide. Thiolated products are prepared by subsequent DTT reduction. Oligonucleotides prepared with SPDP have reactive moieties on linkers of ~10 Å length, while those prepared with LC-SPDP have linkers of ~20 Å. These probes can capture interhelical encounters at distances of ≤20 Å and ≤40 Å, respectively, because each helix bears such a linker. C) Interhelical crosslinking is measured over time by quantitating the radiolabeled thiolated helix by native PAGE.
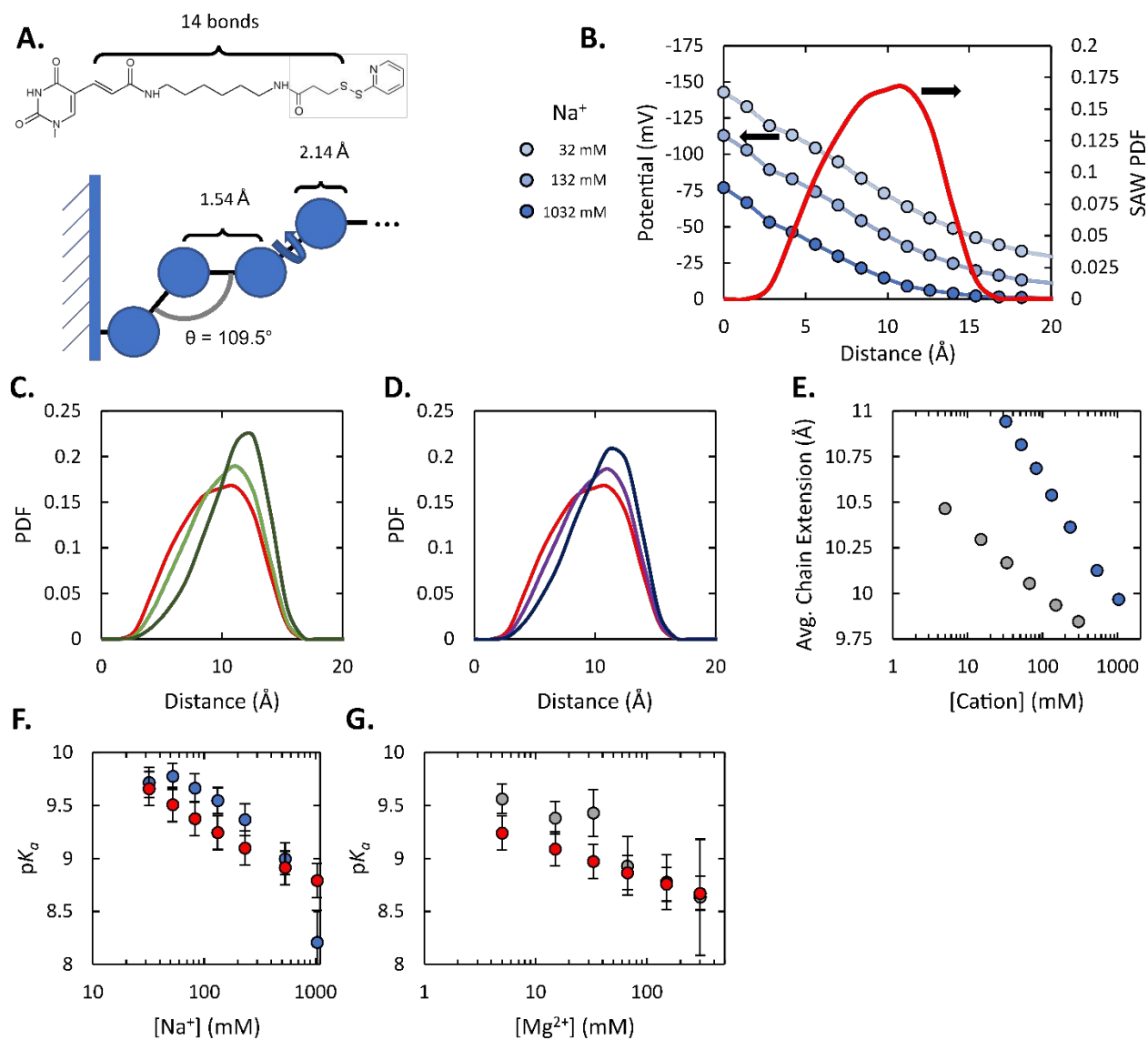
Figure S2. Estimation of average linker extensions by self-avoiding walk (SAW) model. A) The short probe linker was modeled as a freely rotating SAW of 14 segments with fixed bond angle and bond length consistent with C-C bonds. Each segment was modeled as a sphere of approximately the size of a methylene group. One end of the chain was connected to an impenetrable planar surface representing the helix. This model was implemented in Python as a chain growth procedure with simple sampling, and a total of 27,693 unique chain configurations were sampled out of 2.5×10^8 attempted growths. B) The probability distribution function (PDF) of linker ends obtained from the model in A) (red curve) yields an average linker extension of 9.46 Å. The electrostatic potential (modeled by PB, blue points and curves, see also Fig. 1) varies substantially across the width of the PDF, biasing the actual distribution of locations of the thiolated linker, which carries a partial negative charge. C,D) The unperturbed SAW PDF (red) is re-weighted by the electrostatic potentials to yield electrostatically perturbed PDFs in the presence of C) NaCl (dark green, 32 mM; light green, 1 M) and D) $MgCl_2$ (indigo, 5 mM; violet, 300 mM). E) Average chain extensions calculated from electrostatically perturbed PDFs as a function of NaCl (blue) or $MgCl_2$ (grey) concentration. F,G) Thiol pK_a values predicted from potentials calculated by PB and chain extensions calculated from the SAW model (red) correspond reasonably well with actual pK_a measurements across concentrations of F) NaCl (blue) and G) $MgCl_2$ (grey). Error bars show SE of fits for each pK_a determination.

6

A.

Disulfide-modified

5' CGAGGCA**T**CGTGGCC 3'
3' GCTCCGTAGCACCGG 5'

Thiol-modified

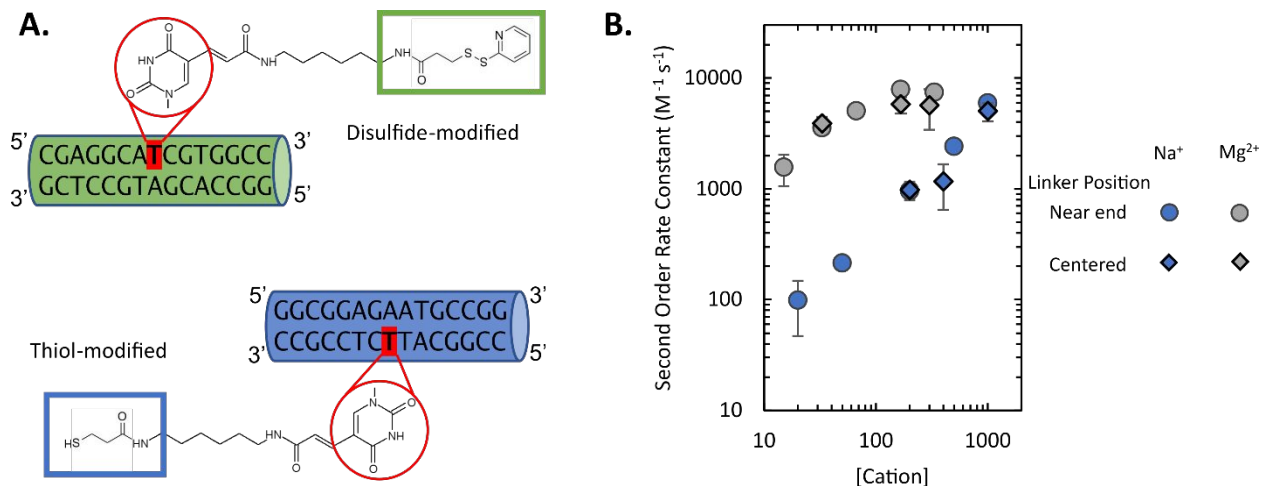5' GGCGGAGAATGCCGG 3'
3' CCGCCTC**T**TACGGCC 5'

B.

Figure S3. For most reactions, linkers were located 3 or 4 bp from the end of each helix (Fig. 2A). A) To test whether the results were influenced by the proximity of the linkers to the helix ends, we also performed some reactions with linkers located at the center of each helix. B) Second-order rate constants of crosslinking with Na^+ (blue) and Mg^{2+} (grey), measured with either centered linkers as in panel A (diamonds) or linkers 3 or 4 bp from the end of each helix (circles). Second-order rate constants were determined from three or more pseudo-first-order rate constant measurements. Error bars show the standard error and are smaller than the symbols in some cases.
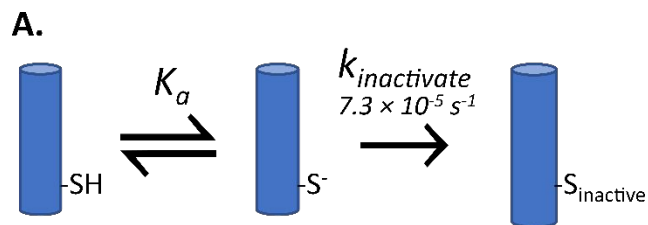
A.

B.
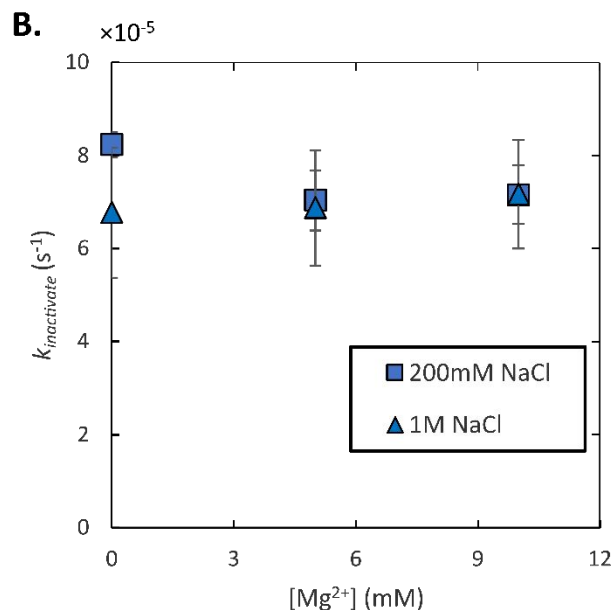
Figure S4. A) A first-order side reaction inactivates the thiol. B) Experiments were designed to measure the thiol-inactivating side reaction by incubating the thiolated helix at pH 9.0 and 37°C with different concentrations of NaCl and MgCl$_2$. Aliquots from these reactions were collected at various times and allowed to rapidly crosslink with a disulfide-labeled helix to completion. The reduction in total reaction amplitude with time of pre-incubation, beyond the ~50% of the thiolated helix that was apparently inactivated prior to the start of reactions (see Fig. 2C), was used to determine the rate constant of inactivation ($k_{inactivate}$). The value of this rate constant was 7.3×10^{-5} s^{-1} and it did not display a systematic dependence on salt concentration. Note that the intercept of the fit line in Fig. 2D does not pass through this value because the intercept is not fixed in the fit. Fixing the intercept does not substantially change the fitted second-order rate. We chose not to fix the intercept because the uncertainty of individual first-order rate measurements was often larger than the rate constant of this side reaction.
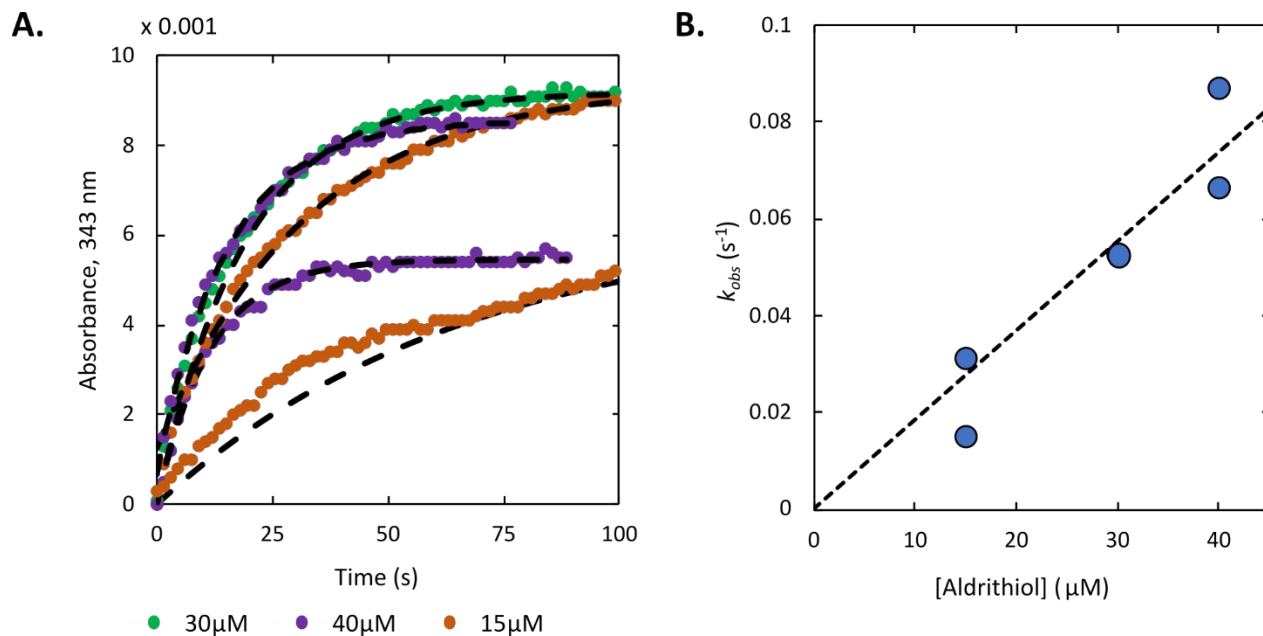
Figure S5. A) Example absorbance time courses for disulfide exchange reactions with 2-aldrithiol. Colors correspond to 2-aldrithiol concentrations, with corresponding exponential fits. All reactions were performed at pH 9.0 (~32 mM ionic strength) with 1.5 μM thiolated helix. Endpoints vary between reactions in a range corresponding to 40 – 70% of the total thiol, using an extinction coefficient for product 2-thiopyridine of 8000 M^{-1} cm^{-1}. Pseudo-first-order rate constants determined from curves in A) are fit linearly in B) to yield a second-order rate constant. All second-order rate constants were determined from at least three pseudo-first-order-rate-constant measurements.

A.

Terminal thiol in crosslinking reactions

DNA

N-phenyl-3-sulfanylpropanamide
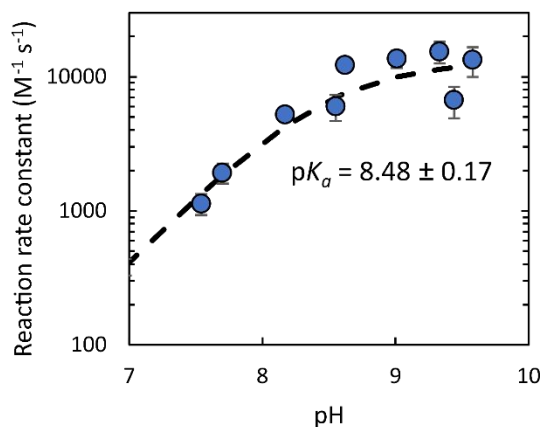
K_a

B.

$pK_a = 8.48 \pm 0.17$
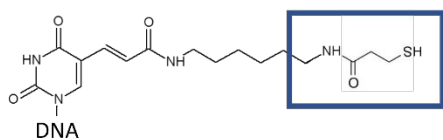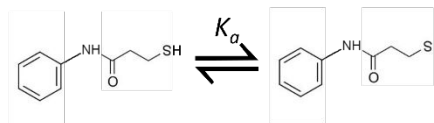
Figure S6. Establishment of a reference pK_a for the free thiol. A) The reagent N-phenyl-3-sulfanylpropanamide (NPSP) was selected as a structural analogue of the terminal thiol present in our crosslinking reactions. B) Disulfide exchange reactions between NPSP and 2-aldrithiol similar to those performed with thiolated DNA (Figs. 3 and S4) across a range of pH values. Blue points are second-order rate constants determined from at least three pseudo-first-order-rate-constant measurements. The black dashed curve is the best fit titration curve, with the same maximal rate constant (1.3×10^4 M^{-1} s^{-1}) as observed for both disulfide exchange and crosslinking with thiolated DNA.
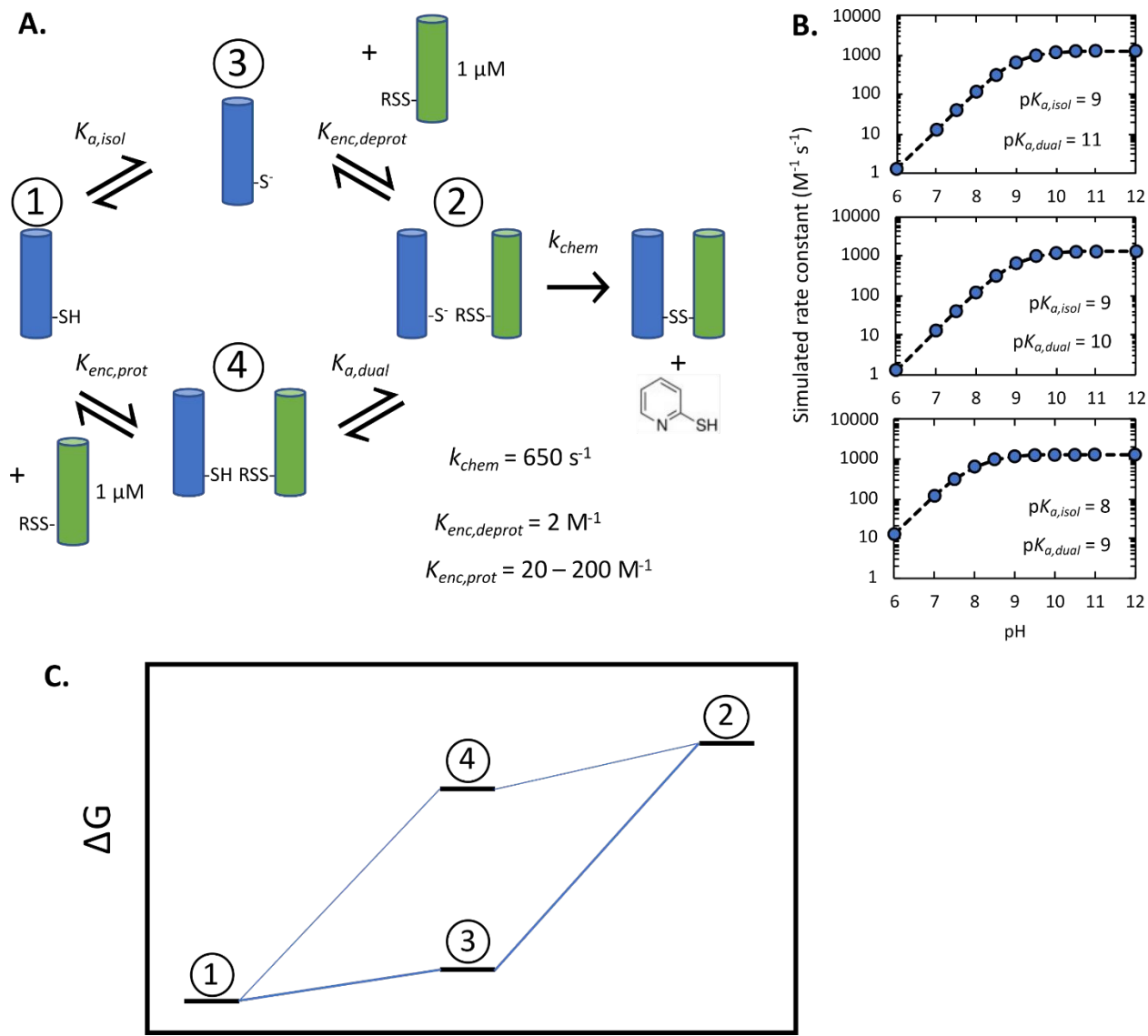
A.

③

+

RSS- 1 μM

$K_{a,isol}$

$K_{enc,deprot}$

①

-SH

-S-

②

-S- RSS-

k_{chem}

-SS-

+

N SH

$K_{enc,prot}$

④

$K_{a,dual}$

+

1 μM

RSS-

-SH RSS-

$k_{chem} = 650 \ s^{-1}$

$K_{enc,deprot} = 2 \ M^{-1}$

$K_{enc,prot} = 20 - 200 \ M^{-1}$

B.

Simulated rate constant ($M^{-1} \ s^{-1}$)

$pK_{a,isol} = 9$
$pK_{a,dual} = 11$

$pK_{a,isol} = 9$
$pK_{a,dual} = 10$

$pK_{a,isol} = 8$
$pK_{a,dual} = 9$

pH

C.

ΔG

② ④ ③ ①

Figure S7. Assessing the impact of helical encounter on the observed thiol pK_a by kinetic simulation. A) The reaction scheme in Fig. 2B is expanded to show that the reversible thiol deprotonation and helical encounter steps may occur in either order prior to disulfide exchange. The top path shows the ordering shown in Fig. 2B, where the relevant pK_a is that of the isolated thiol helix, and interhelical encounters occur with the deprotonated thiol. The bottom path shows an alternate ordering, in which the presence of a second helix may perturb the thiol pK_a, such that $K_{a,isol} \neq K_{a,dual}$. Additionally, because the second helix will locally increase the negative electrostatic potential, it is expected that $K_{a,isol} > K_{a,dual}$. B) The reaction scheme in panel A was numerically simulated using values for equilibrium and kinetic parameters as shown, and overall second-order reaction rates (circles) were determined across pH. For a variety of different combinations of $K_{a,isol}$ and $K_{a,dual}$, the observed pK_a, as determined from the pH dependence of the second-order rate, matched that of the isolated helix (dashed lines show Henderson-Hasselbalch fits assuming $pK_a = pK_{a,isol}$). C) State diagram roughly showing relative free energies of discrete states in A).
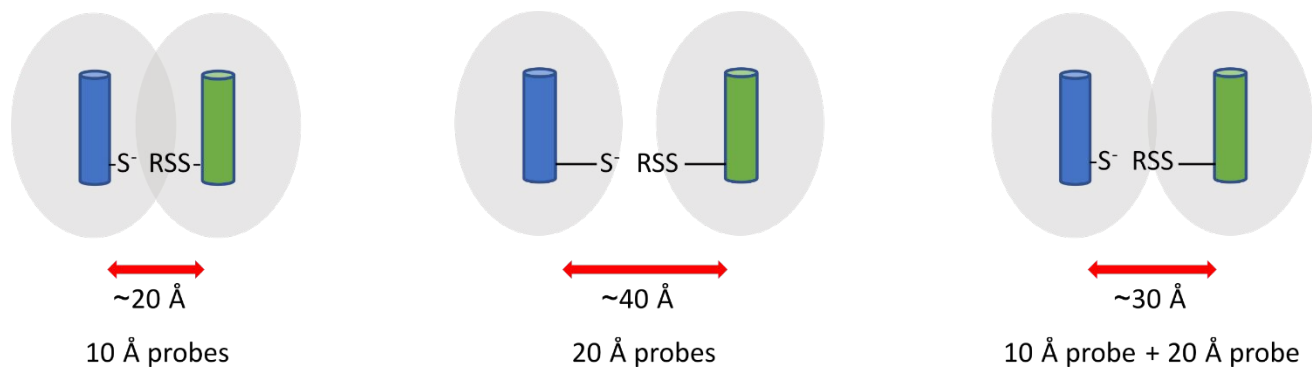
Figure S8. At a given fixed salt concentration, helical encounters at long distances may be nearly or completely electrically screened, while short distance encounters might require overlapping electrostatic fields, leading to substantial electrostatic repulsion. Probing encounters at different separations enables an estimation of the distance that the electrostatic field extends away from the helix.
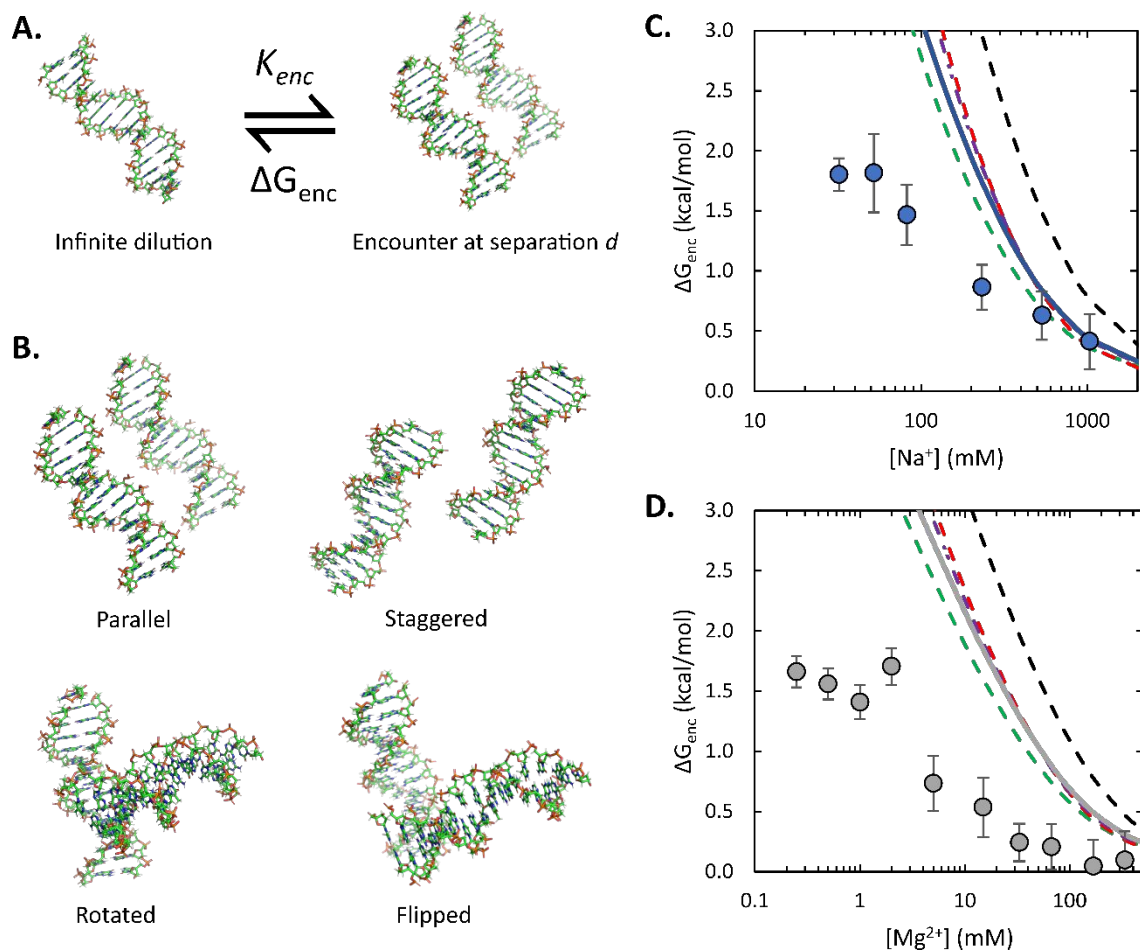
Figure S9. Poisson-Boltzmann calculations of electrostatic free energy of interhelical encounters. A) Poisson Boltzmann calculations are first performed on isolated helices to establish the electrostatic energy on a single helix and its surrounding ions. A separate calculation is done on a pair of helices, and the difference in electrostatic energy is taken as ΔG for the encounter. B) Since ΔG_{enc} may depend on helical orientation, we compute ΔG for four different orientations. The ensemble average of these energies is then taken to be ΔG_{elec}. Panels C) and D) compare experimental ΔG_{enc} (points) with PB calculations (dashed lines) for each of the orientations in B) and their ensemble average (solid lines). For all PB calculations shown, the distance between helices is 20 Å, and in all $MgCl_2$ runs, 32 mM monovalent was explicitly included to match the experimental contribution from buffer. Dashed line colors indicate orientation: green, staggered; purple, flipped; red, rotated; black, parallel.
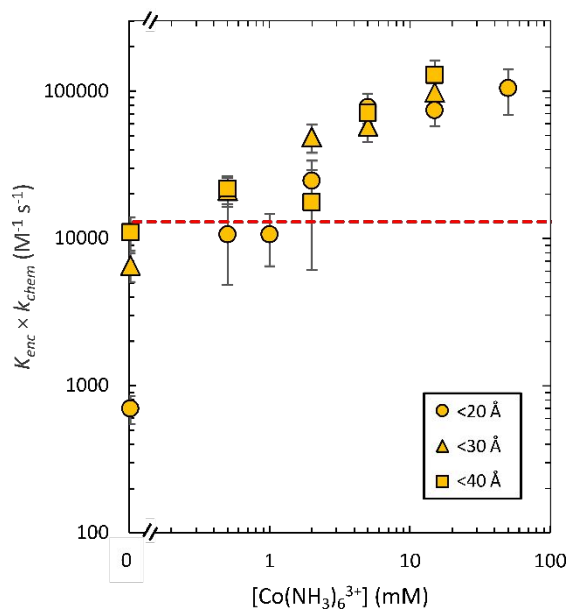
Figure S10. Measured crosslinking rate constants at different probe distances with Co(NH$_3$)$_6$Cl$_3$. Changing the probe distance does not substantially impact the relationship between encounter frequency and concentration, and the magnitude of the attractive potential is the same with all probes, indicating that the attractive well occurs at an interhelical separation <20 Å.
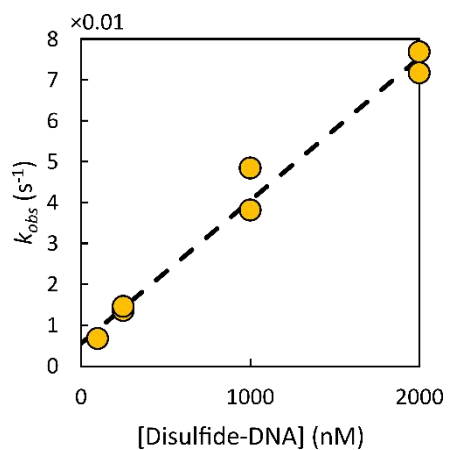
Figure S11. Observed pseudo-first-order crosslinking rate constants vary linearly with disulfide concentration at pH 9.0 with 15 mM $Co(NH_3)_6Cl_3$, a concentration within the attractive regime. These data show that the encounter equilibrium constant K_{enc} carries no higher-order DNA concentration dependence, and thus that the magnitude of interhelical attraction is not DNA concentration-dependent.
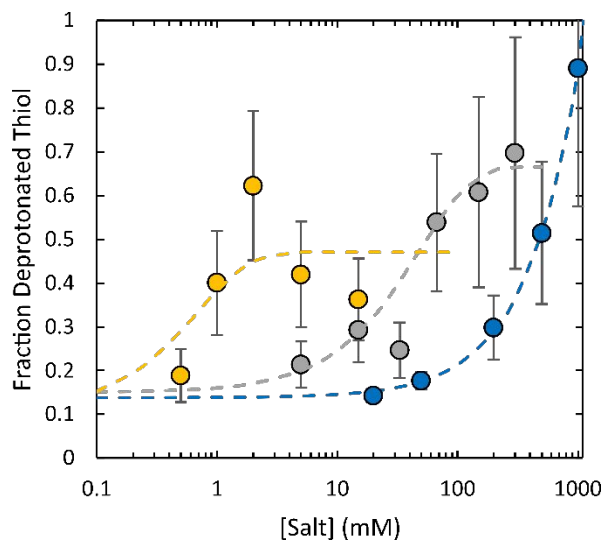
Figure S12. Fraction of deprotonated thiol determined from 2-aldrithiol disulfide exchange rate data. Data were collected at several concentrations of NaCl (blue), $MgCl_2$ (grey) and $Co(NH_3)_6Cl_3$ (yellow). These deprotonation fractions were used to normalize crosslinking data against salt-dependent pK_a effects and obtain crosslinking rate constants for the thiolate. Because 2-aldrithiol data were not collected at all of the salt concentrations used in crosslinking, empirical curve fits (dashed lines) were used to estimate deprotonation fractions across salt concentrations. These curves are empirical and should not be viewed as explicit models of underlying behavior.
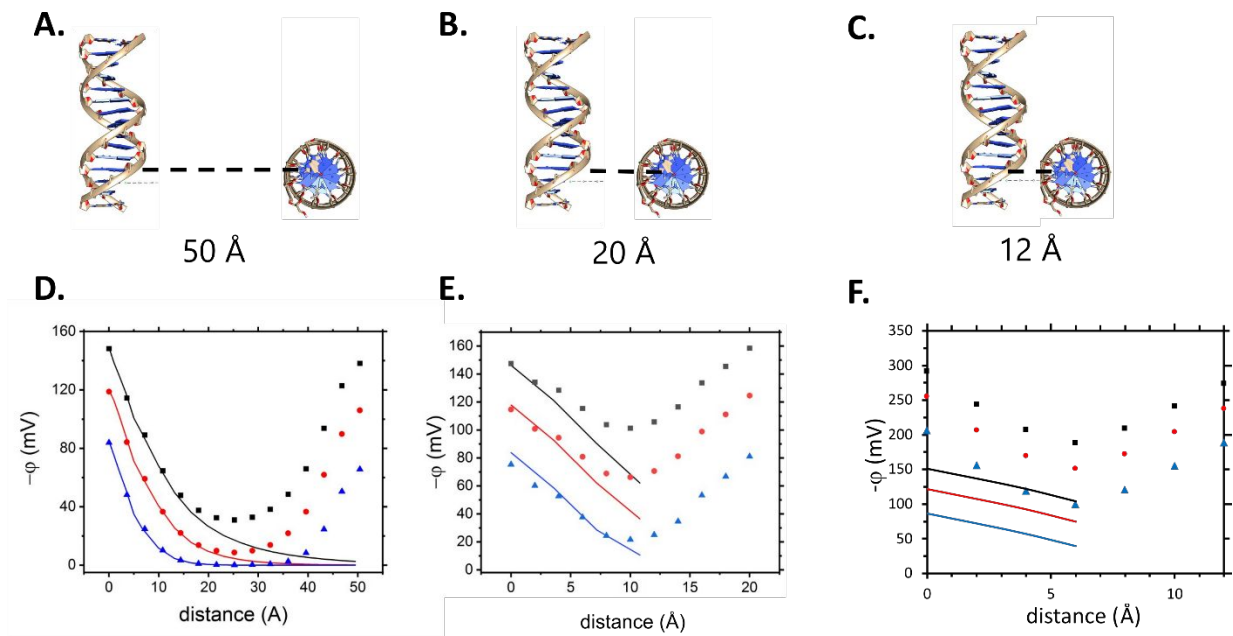
Figure S13. Poisson-Boltzmann (PB) predictions of the electrostatic potential (φ) generated by DNA helices in close proximity in a "flipped" orientation and screened by monovalent ions. In this orientation, the helices are rotated 90° with respect to one another. A-C) Flipped helices at separations of 50, 20, and 12 Å. D-F) PB calculations of electrostatic potential between two helices along coordinates indicated by dashed lines in A-C. Points are potentials between DNA helices and lines are potentials calculated around a singular dsDNA as shown in Fig. 1A,B. Colors represent ion concentrations: black 32 mM, red 132 mM, and blue 1 M. Model building and rendering was done in Chimera. PB calculations were carried out with APBS.

Table S1. Oligonucleotides used in this study. C5-amino-dT is indicated by /iAmMC6T/.

Disulfide helix, short linkers	IHO114	5' CGA GGC AGC GTG /iAmMC6T/CC 3'
	IHO115	5' GGA CAC GCT GCC TCG 3'
Thiol helix, short linkers	IHO116	5' CCG /iAmMC6T/CA TGC TCC GCC 3'
	IHO117	5' GGC GGA GCA TGA CGG 3'
Disulfide helix, mid/long linkers	IHO345	5' GGA GAG GAC GAG ACC 3'
	IHO347	5' GGT CTC GTC CTC /iAmMC6T/CC 3'
Thiol helix, mid/long linkers	IHO340	5' CCA CAC CAG CAC AGG 3'
	IHO343	5' CC/iAmMC6T/ GTG CTG GTG TGG 3'

SI References

(1)   Johnson, K. A.; Simpson, Z. B.; Blom, T. Global Kinetic Explorer: A New Computer Program for Dynamic
        Simulation and Fitting of Kinetic Data. *Analytical Biochemistry* **2009**, *387* (1), 20–29.
        https://doi.org/10.1016/j.ab.2008.12.024.